



Designing the nano-scale architecture of the air electrode for high-performance and robust reversible solid oxide cells

Saeed Ur Rehman^a, Muhammad Haseeb Hassan^{a,b}, Hye-Sung Kim^a, Rak-Hyun Song^{a,b}, Tak-Hyoung Lim^{a,b}, Jong-Eun Hong^a, Dong-Woo Joh^a, Seok-Joo Park^{a,b}, Jong-Won Lee^{c,*}, Seung-Bok Lee^{a,b,**}

^a High Temperature Energy Conversion Laboratory, Korea Institute of Energy Research, 152 Gajeong-ro, Yuseong-gu, Daejeon 34129, Republic of Korea

^b Department of Advanced Energy and System Engineering, University of Science and Technology, 217 Gajeong-ro, Yuseong-gu, Daejeon 34113, Republic of Korea

^c Division of Materials Science and Engineering, Hanyang University, 222 Wangsimni-ro, Seongdong-gu, Seoul 04763, Republic of Korea

ARTICLE INFO

Keywords:

Solid oxide cell
Electrolysis
Green hydrogen
Air electrode
Nanofabrication

ABSTRACT

Herein, an innovative $\text{La}_{0.6}\text{Sr}_{0.4}\text{CoO}_3$ (LSC) nanostructured air electrode, having superior catalytic activity and exceptional robustness against critical interfacial delamination-induced degradation, is reported. A ~ 50 nm thin LSC air electrode decorated onto a porosity graded $\text{Gd}_{0.1}\text{Ce}_{0.9}\text{O}_2$ backbone via ultrasonic-assisted infiltration showed significantly flourished ORR and OER kinetics with prolific electrochemical performance compared to the cell with conventional LSC air electrode. The SOC showed maximum power density of 2.24 W cm^{-2} in the fuel cell mode and maximum current density of 4.57 A cm^{-2} at an operating voltage of 1.6 V in the electrolysis mode at 750°C . Results of the reversible cycling and galvanostatic stability tests indicate excellent durability, which is attributed to the elimination of detrimental O_2 pressure evolved at the air electrode/electrolyte interface. Sited among the highest performances till date, this study provides a realization of a tremendously durable SOC design for the production of green hydrogen and electricity.

1. Introduction

The surge in energy demand is a fundamental cause of the significant reduction in the limited reserves of fossil fuels, e.g., coal, petroleum, and natural gas [1]. The continuous increase in CO_2 emissions caused by the combustion of fossil fuels is seen as a significant driver of global warming and environmental problems [2]. To counter greenhouse emissions, renewable energy sources such as solar and wind have emerged as prospective alternatives for power generation [3]. However, due to the intermittent nature of renewables in electricity generation, rational yet sustainable energy storage and conversion technologies are required. Over the past few decades, hydrogen, being sufficiently suitable and abundant, has attracted significant attention as a major energy carrier. In relation to this, high-temperature steam electrolysis has emerged as a clean, viable, and efficient technology to produce green hydrogen [4–6].

A reversible solid oxide cell (SOC) is a well-admired technology that

offers the distinctive promise of energy generation and storage at the same time. While operating in the fuel cell (FC) mode, the chemical energy of various fuels, e.g., H_2 , syngas, NH_3 , and hydrocarbons, can be converted into electrical energy. For energy storage, SOC is operated in the electrolytic cell (EC) mode, where renewable energy is converted into chemicals. An SOC is composed of two porous electrodes and a dense oxygen ion-conducting electrolyte sandwiched between them [7, 8]. Conventionally, the air electrode consists of strontium-doped lanthanum magnetite (LSM) or a composite of LSM and yttria-stabilized zirconia (YSZ), whereas the fuel electrode is commonly made up of nickel-YSZ cermet [9,10]. However, during long-term operation in the EC mode, considerable physicochemical degradation occurs, which eventually reduces the overall performance of the cell: namely, electrode poisoning by gaseous phases and disruptive interfacial delamination of air electrodes [11].

In particular, cracking and delamination along the air electrode/electrolyte interfaces overshadow several proven advantages of SOC

* Corresponding author.

** Corresponding author at: High Temperature Energy Conversion Laboratory, Korea Institute of Energy Research, 152 Gajeong-ro, Yuseong-gu, Daejeon 34129, Republic of Korea.

E-mail addresses: jongwonlee@hanyang.ac.kr (J.-W. Lee), sblee@kier.re.kr (S.-B. Lee).

<https://doi.org/10.1016/j.apcatb.2023.122784>

Received 5 December 2022; Received in revised form 17 April 2023; Accepted 18 April 2023

Available online 20 April 2023

0926-3373/© 2023 The Authors. Published by Elsevier B.V. This is an open access article under the CC BY-NC-ND license (<http://creativecommons.org/licenses/by-nc-nd/4.0/>).

[12–14]. The SOFC consisting of an LSM-YSZ air electrode showed severe performance degradation of 0.952 V kh^{-1} for galvanostatic operation for 420 h at 1 A cm^{-2} . Although a reversible cycling strategy was proposed to mitigate the microstructural degradation, there might be practical challenges in the EC mode [15]. The delamination of air electrodes is mainly caused by the development of high internal oxygen pressures near the electrolyte/air electrode interface due to oxygen ion oxidation at defect sites and/or closed pores [8,12,14,16–21]. The formation of secondary phases is also responsible for mechanical degradations of the electrolyte/air electrode interface; however, the driving force behind this phenomenon is the high oxygen pressure in that area [13]. Mixed ionic/electronic conducting (MIEC) materials such as $\text{La}_{0.6}\text{Sr}_{0.4}\text{CoO}_3$ (LSC), $\text{La}_{0.6}\text{Sr}_{0.4}\text{Co}_{0.2}\text{Fe}_{0.8}\text{O}_3$ (LSCF), and $\text{Ba}_{0.5}\text{Sr}_{0.5}\text{Co}_{0.2}\text{Fe}_{0.8}\text{O}_3$ (BSCF) are found to ameliorate degradations to some extent owing to their low polarization resistances as compared to those of electronic conducting LSM [5]. On the other hand, a versatile and practical approach of catalyst infiltration has been widely adopted to achieve a high and stable performance of the SOCs. Infiltration of MIEC nanoparticles into LSM-based electrodes or electrolyte backbones has been reported to provide better electrochemical activity and stability [22–28]. For example, the infiltration of $\text{SrTi}_{0.3}\text{Fe}_{0.6}\text{Co}_{0.1}\text{O}_{3-\delta}$ catalysts into an LSM-YSZ air electrode resulted in two-fold enhancement in performance and successfully avoided air electrode delamination for 800 h of continuous galvanostatic operation at 750°C and 0.5 A cm^{-2} [29]. $\text{Sm}_{0.55}\text{Sr}_{0.5}\text{CoO}_{3-\delta}$ was synthesized by infiltration onto the YSZ backbone as an air electrode; however, stability data were provided for only 100 h [30,31]. A $\text{La}_{0.6}\text{Sr}_{0.4}\text{FeO}_{3-\delta}$ nanoparticulate air electrode was fabricated onto the YSZ backbone, but stability data for only 120 h were reported [32]. An LSC air electrode fabricated onto the GDC backbone initially performed well but degraded rapidly during the stability test [33]. Although infiltration technologies have been explored to solve the problems with air electrode degradation by delamination, more extensive research is still needed to mature the technology.

From a fundamental viewpoint, however, it would be critical to either eliminate closed porosity or to ensure that the closed pores are free of any catalyst phases for the oxidation of oxygen ions. In the current study, the associated problem of air electrode delamination is addressed through a rational design of the air electrode: (i) MIEC (LSC) nanolayer, (ii) catalyst-free closed pores, and (iii) graded porous structure. To function as an air electrode, a nanolayer of the LSC catalyst is deposited onto a pre-sintered $\text{Gd}_{0.1}\text{Ce}_{0.9}\text{O}_2$ (GDC) scaffold by ultrasonic-assisted infiltration [34,35]. Among state-of-art SOC air electrode materials (LSM, LSCF, and LSC), LSC was chosen as the air electrode material because of its high activity and MIEC nature [36–39]. The extremely fast diffusion properties of the LSC nanolayer can prevent the development of oxygen pressure at the GDC/LSC interface. Given that the infiltration solution cannot penetrate into the closed pores of the GDC scaffold, the LSC catalyst is deposited only onto the open pores, which should help circumvent delamination. A porosity-graded structure of the GDC scaffold, on the other hand, is used to maximize the reaction sites for the oxygen reduction/evolution process near the electrolyte surface (fine-porosity zone) while allowing for easy mass transport near the air electrode surface (coarse-porosity region). The efficacy of the nanostructured LSC air electrode in improving the performance and stability of reversible SOC is demonstrated in both FC and EC modes.

2. Experimental

2.1. Fabrication of SOCs with nanolayered and conventional LSC air electrodes

Nanolayered LSC air electrodes were fabricated by screen printing and infiltration techniques onto in-lab prepared symmetric and anode-supported half-cells (NiO-YSZ/YSZ) (Kceracell, South Korea). To fabricate the symmetric cells, fully dense YSZ coins were prepared by dry

pressing YSZ powder (YSZ8-TC, Fuelcellmaterials, USA) into circular disks, followed by sintering at 1400°C in air for 5 h. A GDC scaffold with a graded porous structure was fabricated onto the YSZ symmetric cell and the anode-supported half-cell by screen printing, followed by sintering in air at 1300°C for 1 h. After sintering, the porosity-graded GDC scaffold had an active area of 0.5 cm^2 . A graded porous structure was created by screen printing of a GDC ink without any pore-former (70 wt % GDC powder) to produce fine porosity at the interface with the YSZ electrolyte, while a coarse porous structure at the electrode surface was generated by using a GDC ink containing polymethyl methacrylate (PMMA) particles (weight ratio of GDC and PMMA = 70:30). Screen printing inks were prepared in a centrifugal mixer by dispersing powders into a mixture of α -Terpineol (solvent), ethyl cellulose (binder), and fish oil (dispersant). The LSC infiltration solution was prepared by dissolving stoichiometric amounts of high-purity nitrate salts of the precursor elements, i.e., $\text{La}(\text{NO}_3)_3 \cdot 6 \text{ H}_2\text{O}$, $\text{Sr}(\text{NO}_3)_2$, and $\text{Co}(\text{NO}_3)_2 \cdot 6 \text{ H}_2\text{O}$ (Sigma Aldrich, South Korea), in deionized (DI) water, and the solution volume was adjusted to 25 ml. In a separate beaker, an appropriate amount of glycine amino acid (Sigma Aldrich, South Korea) was dissolved in DI water to function as a complexing agent (molar ratio of glycine to metal cations = 0.7: 1.0), and the solution volume was adjusted to 25 ml [40]. The glycine solution was added to the metal nitrate solution slowly while the temperature was kept at 80°C . At this point, 1.5 g of triton X-100 was dissolved in 50 ml of the metal nitrate solution to promote the wettability of the infiltration solution [41]. To find the optimal amount of the LSC, the precursor solution was infiltrated into the GDC scaffold of the YSZ symmetric cells for 1–4 cycles. Infiltration was done by using in-house ultrasonic spray equipment [35,42]. After each infiltration cycle, the sample was heat treated at 200°C , and a final heat-treatment step was performed at 800°C to form the LSC perovskite phase. After finding the appropriate number of infiltration cycles by studying the electrochemical properties of the symmetric cells, the LSC precursor solution was infiltrated into the GDC scaffolds fabricated onto the anode-supported half-cells.

For the fabrication of conventional LSC-GDC composite cathodes, screen printing inks of GDC buffer layer (57 wt% GDC), LSC-GDC (60:40 in weight) composite electrode (air electrode functional layer), and LSC current-collection layer were prepared. A GDC buffer layer was first screen-printed onto the fully dense YSZ electrolyte of the YSZ symmetric cell and the anode-supported half-cell and sintered in air at 1300°C for 1 h. Then, LSC-GDC air electrode functional layer and LSC current-collection layer were screen-printed on the GDC buffer layer successively and sintered in air at 950°C . After sintering, the LSC-GDC composite air electrode had an active area of 0.5 cm^2 .

2.2. Material and electrochemical characterization

The microstructure of the LSC air electrodes was observed by SEM (Hitachi Regulus 8220). The phase of the LSC air electrode formed after calcination at 800°C was confirmed by XRD (2500 D/MAX, Rigaku) using $\text{Cu K}\alpha$ radiation. The surface chemistry of the synthesized nanolayered LSC air electrode was observed by X-ray photoelectron spectroscopy (XPS, Thermo Multi-Lab 2000 spectrometer). Raman spectra of the synthesized nanolayered LSC air electrode GDC powders was collected using Nanophoton Ramanforce dispersive Raman spectrometer (532.04 nm excitation wavelength, 3.82 mW excitation power) over the range of $87\text{--}1000 \text{ cm}^{-1}$. A chemical composition analysis with EDS in STEM was carried out using a Talos F200X device operated at 200 kV. Specimens for the TEM observation were prepared by a lift-out technique via ion-beam thinning in a focused-ion-beam system (Helios G4 UX, Thermo Fisher Scientific). A protective thin layer of Pt was applied over the region of interest to enhance the mechanical strength. $\text{La-L}\alpha$ (4.65 keV), Sr-L (1.82 keV), $\text{Co-K}\alpha$ (6.93 keV), $\text{Ce-L}\alpha$ (4.84 keV), and $\text{Gd-L}\alpha$ (6.05 keV) lines were selected during the EDS analyses with a chemical scanning time of 180 s. A narrow peak area (55%) of the elemental spectrum was applied for La and Ce for easier deconvolution.

The SAED pattern and the inter-planar distance of the crystal were analyzed using DigitalMicrograph™ (GATAN) software. The electrochemical performance of the SOC was measured using an in-house testing rig, as shown in Fig. S1. For this test, a coin cell was mounted onto an alumina tube and sealed using a glass ring. NiO and LTCCC (low temperature cathode current collection) pastes were used to create electrical contacts for the fuel and air electrodes, respectively. Ag mesh and wire were used for the current collection. For FC operation, 0.1 lpm of dry hydrogen was supplied to the Ni-YSZ anode, while the cathode was provided with 0.15 lpm of dry air. For EC testing, the Ni-YSZ anode was supplied with 0.1 lpm of a gas containing 50% steam and 50% hydrogen using a steam generator. *I*-*V* and electrochemical impedance data were collected at 650, 700, and 750 °C using a BioLogic SP-240 electrochemistry workstation. Electrochemical impedance was

conducted by employing a 14 mV_{rms} AC signal in a frequency range of 0.01 Hz to 100 kHz.

3. Results and Discussion

The SOC air electrode is commonly fabricated by the screen printing and sintering of single or composite materials, which unavoidably produces closed pores between the catalyst particles. Operating the SOC in the EC mode results in the evolution of oxygen gas that should diffuse out of the air electrode. The encapsulated oxygen gas inside the closed pores has the potential to deteriorate the mechanical integrity of the air electrode, thereby causing delamination (Fig. 1a). By employing an ultrasonic-assisted infiltration technique, in this study, the SOC air electrode is designed and fabricated in such a way that there is no

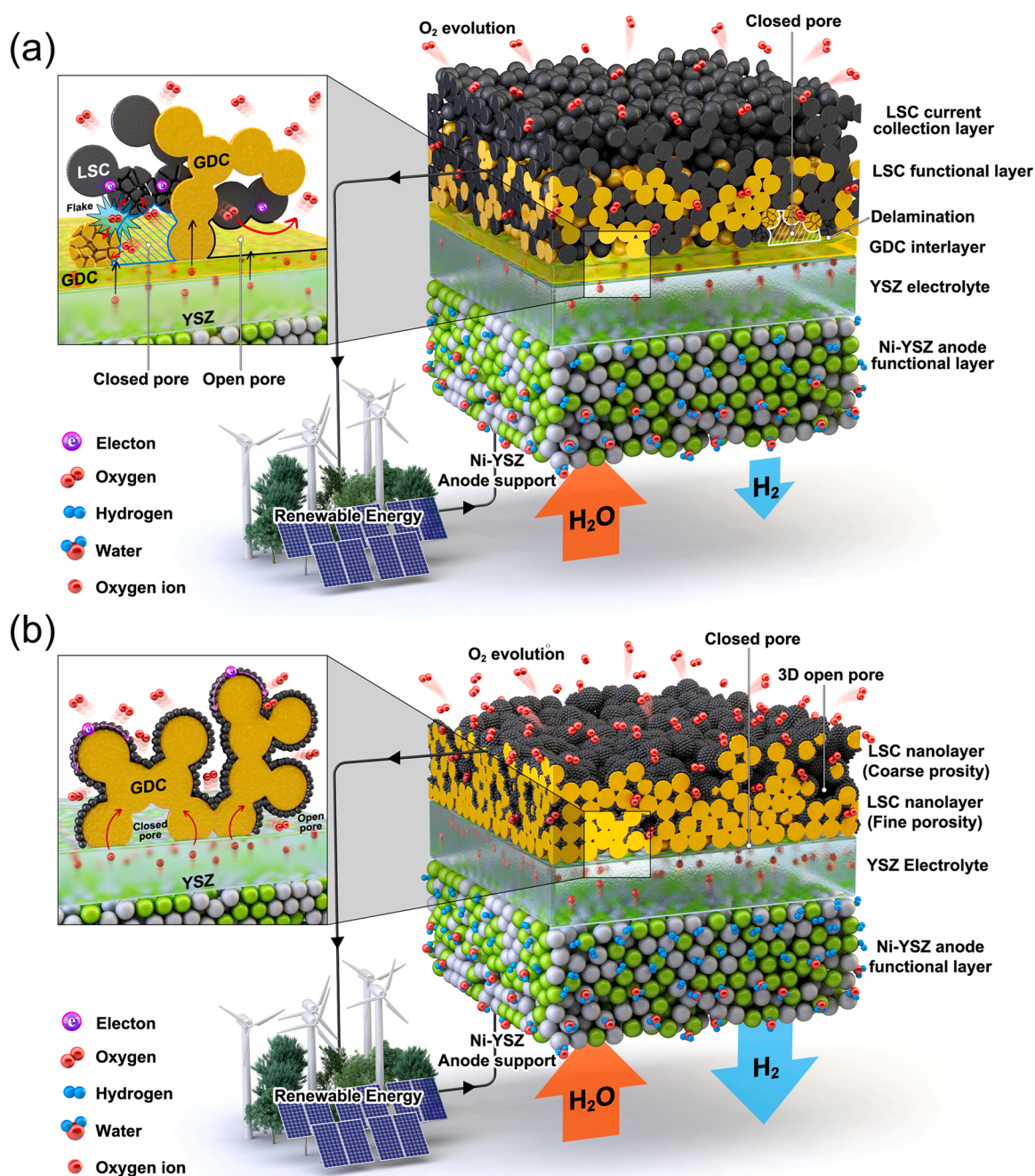


Fig. 1. Schematic illustration comparing SOC structures and their effects on performance and long-term stability: (a) a conventionally prepared LSC-GDC composite air electrode and (b) the developed LSC nanolayered air electrode.

catalyst inside the closed pores (Fig. 1b).

3.1. Nanolayered LSC air electrode synthesis on GDC buffer layer free SOC

In a conventional SOC configuration, a GDC buffer layer between the air electrode and zirconia-based electrolytes is required to inhibit cation inter-diffusion during high-temperature sintering (Fig. 1a) [43–45]. In the present study, the relatively low calcination temperature of the infiltrated LSC allows for the design and fabrication of the SOC without a GDC buffer layer (Fig. 1b). A graded porous structure was also implemented for the GDC scaffold, which was composed of a fine porous structure near the interface with the YSZ electrolyte and a coarse porous structure at the GDC surface (Fig. 1b). The fine porous structure on the electrolyte side can enlarge the electrochemical active area, i.e., the LSC surface available for the oxygen reduction/evolution reaction, and at the same time it enables easy access to oxygen ions, thus contributing to the reduction in the charge-transfer resistance of the air electrode. On the other hand, the benefits of large pores formed in the electrode surface region is twofold. First, they facilitate the diffusion of the oxidant and reduce the concentration polarization in the FC mode. Secondly, they can assist in minimizing the stress on the air electrode by facilitating the oxygen evolution process in the EC mode. In addition, superior sinterability, high thermal expansion coefficient, and the highly reactive nature of the LSC phase make it challenging to fabricate mechanically robust air electrode/electrolyte interfaces via sintering at a high temperature [43,46]. Unlike the conventional fabrication method, the GDC scaffold is sintered prior to the impregnation of the LSC phase [47,48]. Thus, a high-temperature sintering process can be used for the fabrication of GDC scaffolds (1300 °C in the present study) enabling strong mechanical interlocking between the air electrode and electrolyte [49].

In this study, an LSC catalyst was synthesized onto a GDC scaffold in only a couple of ultrasonic-assisted infiltration cycles that involved a low-temperature heat-treatment (200 °C) and final calcination (800 °C), as illustrated in Fig. 2. Here, glycine was used as a complexing agent in combination with a surfactant to (i) obtain a pure LSC phase at a relatively low calcination temperature and (ii) minimize the amount of catalyst required to achieve sufficient percolation of LSC. In the absence of a complexing agent, the metal ions would precipitate out at different rates during the drying process, depending on the solubility limit of each metal salt. Glycine inhibits the undesirable precipitation of metal ions by entrapping them upon drying and provides highly stoichiometric mixing of the precursor elements, leading to the formation of a desired phase with high crystallinity at a significantly reduced temperature. Triton X-100 was therefore added into the infiltration solution to improve its wettability (surfactant) and to facilitate the formation of pure crystallites (complexing agent) [50–55]. The modified precursor solution was proven to spread over the entire surface of the GDC scaffold and infiltrate into the fine pores that are located deep on the electrolyte side.

3.2. Microstructure of nanolayered LSC air electrode

Fig. 3a illustrates the microstructure of the cell before the infiltration of the LSC catalyst, where a dense NiO-YSZ anode functional layer

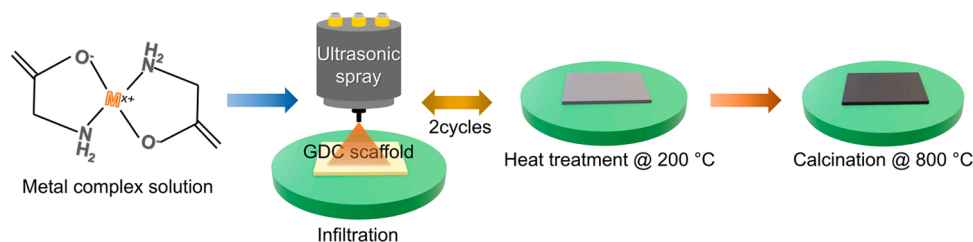


Fig. 2. A schematic of the ultrasonic-assisted infiltration process used to synthesize a nanolayered LSC air electrode for SOCs.

(AFL), a highly dense YSZ electrolyte layer, and a pristine GDC scaffold with a graded porous structure can be observed (see the elemental mapping results in Fig. S2). Porosities of the GDC scaffold were estimated to be 33.9% for the fine porosity layer located at the interface with the YSZ electrolyte and 54.7% for the coarse porosity layer located at the interface with the air (Fig. S8a, b, and Table S1). Cross-sectional scanning electron microscopy (SEM) images (Fig. 3b) and elemental mappings (Fig. S3) of the SOC obtained after the LSC infiltration and calcination show the uniform distribution of the precursor elements, i.e., La, Sr, and Co, within the GDC scaffold. The two different regions (indicated by squares) near the surface of the air electrode and the air electrode/electrolyte interface are enlarged in Fig. 3c and d, respectively. For a better understanding, the fresh GDC surfaces exposed after sample cutting for SEM analysis (Fig. 3c and d, S6b) are designated in yellow in Supplementary Fig. S7. This clarifies that during the infiltration process, the LSC covers the whole surface of the GDC scaffold.

Moreover, Fig. S4 presents a high-angle annular dark-field (HAADF) image of the nanolayered LSC air electrode and the corresponding compositional maps acquired by scanning transmission electron microscopy (STEM) and energy-dispersive X-ray spectroscopy (EDS). The SEM and STEM observations clearly indicate that the infiltration strategy adopted in this research produces LSC catalyst with high stoichiometric uniformity onto the GDC scaffold. In general, an MIEC catalyst possesses an extended utilization length, when compared to the commonly used electronic conductors such as LSM. Therefore, the LSC nanolayer on the GDC scaffold can provide the entire surface as a two-phase boundary for the oxygen reduction/evolution reaction, thereby expanding the electrochemically active surface [56]. Also, the LSC nanolayer exhibits a significantly reduced resistance to the transport of oxygen ions, enhancing the reaction kinetics of the air electrode [57,58].

For comparison, a standard design SOC with a GDC buffer layer and an LSC-GDC composite air electrode was fabricated using conventional screen printing and sintering processes (Fig. S5). Fig. S6 shows a noticeable difference between the microstructures of SOFCs consisting of the nanolayered LSC and conventional LSC-GDC composite air electrodes. Porosity of the LSC-GDC composite air electrode was estimated to be 32.3% (Fig. S8c, Table S1).

3.3. Phase, surface chemistry, and chemical composition of nanolayered LSC air electrode

The LSC nanolayer synthesized via infiltration must constitute a pure perovskite phase to function as a high-performance and stable air electrode. An X-ray diffraction (XRD) analysis was carried out on the infiltrated LSC air electrode (calcined at 800 °C) to verify the formation of the pure perovskite phase, as shown in Fig. 4a. The XRD patterns indicate the presence of YSZ and GDC phases, which exist in major amounts. The major peak (110) for LSC overlaps the (220) peak for GDC; however, the minor peaks indicated by the arrows substantiate the existence of LSC. The XRD patterns of LSC are in good agreement with the standard XRD data of $\text{La}_{0.6}\text{Sr}_{0.4}\text{CoO}_{3-x}$ (ICDD 48–0121). It is noteworthy that there is no indication of any secondary phases, proving the stoichiometric distribution of the precursor elements in the LSC nanolayer. Hence, the XRD results of the LSC nanolayer fabricated onto the GDC

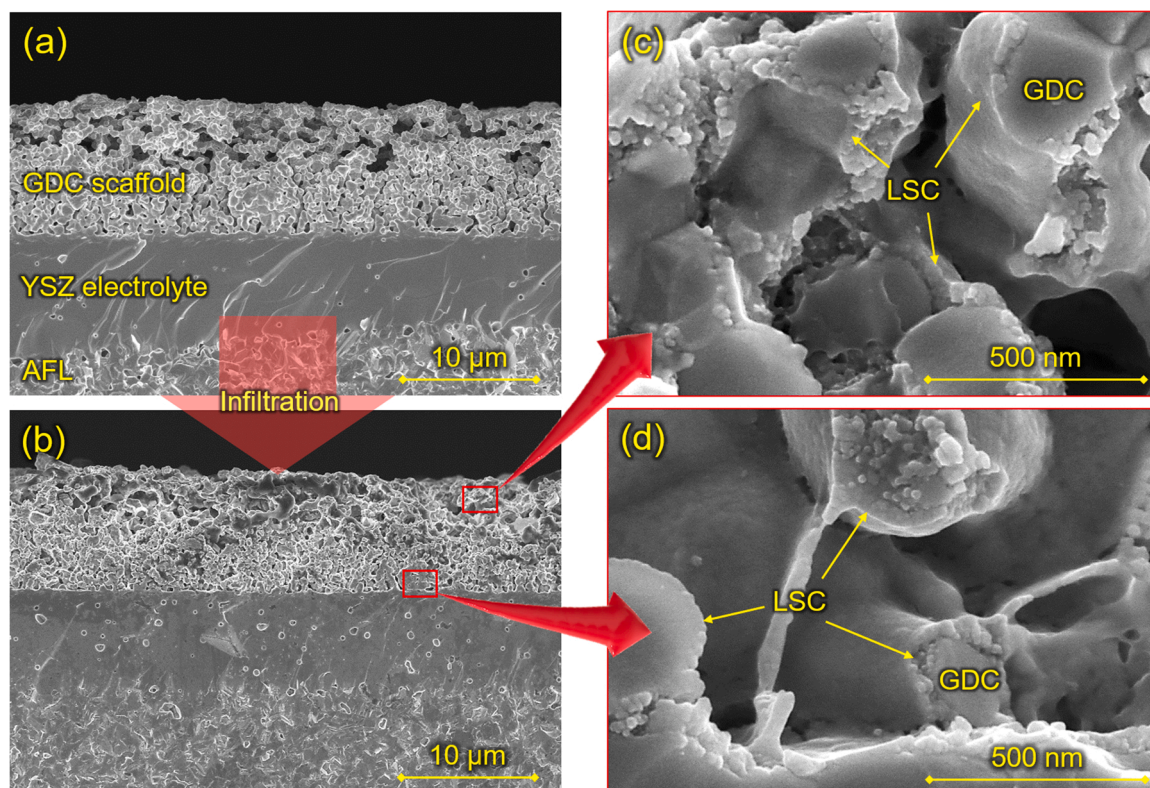


Fig. 3. Cross-sectional SEM images of (a) the SOC with a pristine porosity-graded GDC scaffold and (b) the SOC with a nanolayered LSC catalyst deposited onto a porosity-graded GDC scaffold. (c) and (d) show high-resolution SEM images corresponding to the insets near the electrode surface and the interface with the YSZ electrolyte, respectively.

scaffold confirm the formation of a pure LSC phase with a highly crystalline perovskite structure.

The surface chemistry of the synthesized nanolayered LSC air electrode was observed by XPS analysis (Fig. S9a, b). Fig. S9a illustrates the survey scan of the nanolayered LSC air electrode, which shows the presence of the constituting elements of the LSC and GDC phases. Fig. S9b shows the high-resolution O1s spectrum, consisting of two peaks located at 528.4 and 531.5 eV. The peak located at 528.4 eV shows the presence of oxygen in the LSC lattice, whereas the peak at 531.5 eV indicates the presence of oxygen species adsorbed at the LSC surface [59]. The absence of the peaks related to secondary phases demonstrates the formation of a pure LSC phase. A Raman spectrum was also taken from the surface of the nanolayered LSC air electrode, as shown in Fig. S9c. The Raman spectrum shows the presence of the GDC phase as indicated by a sharp active vibrational mode at 459 cm^{-1} [60]. However, the Raman spectrum did not show the features of the LSC surface because the cubic perovskite phase of the LSC has little Raman activity [61–64].

The formation of the pure LSC phase was investigated further by carrying out a detailed transmission electron microscopy (TEM) analysis of the LSC nanolayer. The STEM-EDS characterization was conducted to examine the elemental distribution within the LSC nanolayer on the GDC scaffold. Fig. 4b presents an atomic-scale HAADF image of the LSC nanolayer, which shows the (110) plane of the perovskite phase with an average lattice inter-planar spacing of $d_{110} = 3.971\text{ Å}$. A minor difference in the d_{110} value between the observed and standard (3.870 Å) might be attributed to wet processing, which can create minute compositional variations along the position, as indicated by the lattice parameter calculated spanning a 3.5 nm range (Fig. S10). The selected area electron diffraction (SAED) pattern for the boxed area in Fig. 4b proves the long-range ordered crystal structure. Furthermore, Fig. 4c presents the atomic-scale HAADF-STEM mappings carried out to investigate the elemental distribution inside the LSC. The locations of the La,

Sr, and Co atoms are indicated in the HAADF image. La and Sr atoms located on the A-sites of ABO_3 -type perovskite were found to be brighter as compared to Co located on the B-sites. The STEM-EDS mappings indicate the appreciable uniformity of the elemental distribution over the LSC nanolayer at the atomic scale. This aspect was also supported by the La+Co and Sr+Co overlapped images, which provide additional evidence of the highly stoichiometric characteristics of the LSC nanolayer. In addition, the ordering of the elements at the A and B-sites can be observed in the STEM-EDS mapping images.

3.4. Superior FC-mode performance of SOC comprising of nanolayered LSC air electrode

Four symmetric cells were prepared for which the LSC nanolayered air electrode was synthesized with 1, 2, 3, and 4 infiltration cycles of the precursor solution. Symmetric cells were tested at 700 °C to determine the optimal LSC loading (Fig. S11). A symmetric cell consisting of the conventional LSC-GDC composite cathode was also tested for comparison. The Nyquist and Bode plots obtained from the impedance data (Fig. S11a and b) showed that a maximum performance ($R_p = 0.19\text{ Ω cm}^2$) was obtained when the nanolayered LSC air electrode was synthesized with two infiltration cycles. In comparison, the symmetric cell with a conventional LSC-GDC composite air electrode showed a large impedance arc ($R_p = 0.35\text{ Ω cm}^2$). Based on the results obtained for the symmetric cells, the nanolayered LSC air electrode for the anode-supported SOC was prepared by employing two infiltration cycles of the precursor solution.

Fig. 5 compares the electrochemical performance of the anode-supported SOC with the nanolayered LSC and conventional LSC-GDC air electrodes in the FC mode. The current (I) vs. voltage (V) data were measured at the operating temperatures of 650 , 700 , and 750 °C using dry hydrogen as a fuel and air as an oxidant, as shown in Fig. 5a. The open-circuit voltage (OCV) values obtained at different operating

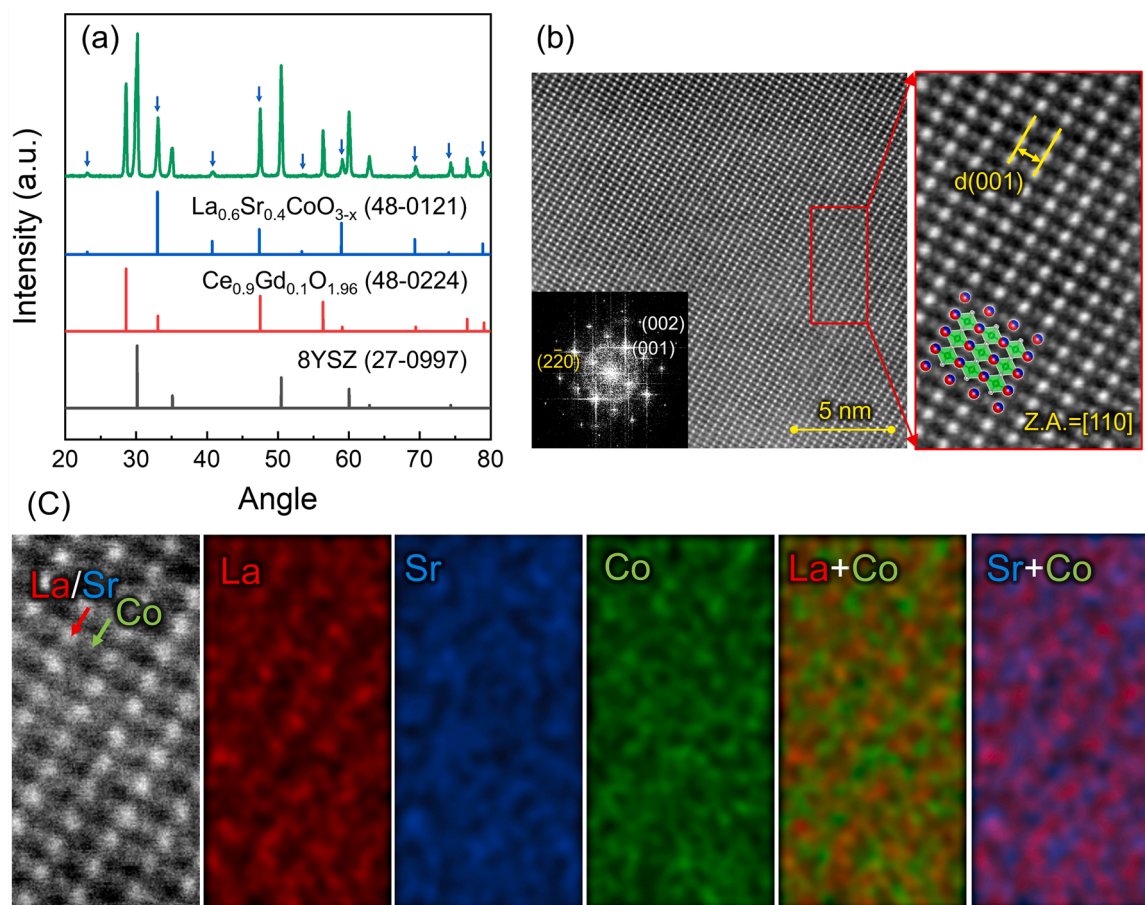


Fig. 4. (a) XRD patterns, (b) HAADF TEM images, and (c) STEM-EDS elemental mappings of the nanolayered LSC air electrode on the GDC scaffold.

temperatures for both SOC are close to the Nernst potential values (> 1.1 V), which indicate adequate gas tightness of the sealing and electrolyte. The values of maximum power density (MPD) for the SOC with the nanolayered LSC are as high as 2.24, 1.42, and 0.82 W cm^{-2} at 750, 700, and 650°C , respectively, which are much higher than those of the SOC with the conventional LSC-GDC composite (1.36 , 0.85 , and 0.48 W cm^{-2}), correspondingly. Fabricating the LSC air electrode as a nanolayer onto the GDC scaffold brings about a prominent performance boost of 64.7%, 67.0%, and 70.8% at corresponding operating temperatures. The FC mode electrochemical performance comparison of the two SOC is summarized in Table S2. Fig. 5b shows Nyquist plots of the AC-impedance spectra obtained from the two SOC at various temperatures, whereas Fig. 5c provides a comparison of the ohmic and polarization resistances acquired from the impedance data. It can be observed that the ohmic and polarization resistances were significantly reduced in case of SOC with innovative nanolayered LSC air electrode, which concurrently explains the improvement in the cell power density.

The kinetics of various electrochemical processes taking place in the SOC were analyzed by calculating the distribution of the relaxation times (DRT) plots, as shown in Fig. 5d. The DRT plots reveal the presence of six individual processes, termed P1 through P6. P1 signifies the charge-transfer process in the MIEC air electrode and interfaces [65], whereas P2 denotes the charge-transfer reaction and hydrogen oxidation reaction on the AFL [66]. While P2 does not appear to be affected by the air electrode design, the smaller value of the resistance for P1 suggests that the nanolayered LSC catalyst plays a vital role in enhancing the charge-transfer kinetics of the air electrode. The DRT plots indicate a substantial reduction in the area under the curve for P3, P4, and P5 related to the air electrode reactions (surface exchanges of oxygen species, oxygen reduction, and oxygen ion diffusion) [65,67,68]. This

might be explained by a larger active area and reduced resistance for oxygen ion diffusion of the nanolayered LSC as compared to the conventional LSC-GDC composite. The P6 peak located at the lowest frequency region is related to the transport of gaseous species. It is observed that there is no noticeable difference in the height of the peak P6 in both cases, suggesting that a difference in the porosity of the two air electrodes had no significant influence on the electrochemical performance. Accordingly, we can conclude that the performance enhancement observed for the SOC with nanolayered LSC is ascribed to the superior charge-transfer and oxygen reduction reaction characteristics of the nanolayered LSC air electrode.

3.5. Superior EC-mode performance of SOC with nanolayered LSC air electrode

Fig. 6 shows an EC-mode electrochemical performance comparison of the two SOC with the conventional LSC-GDC composite and the nanolayered LSC air electrodes (see Table S3 for point-by-point comparison). The EC-mode performance tests were conducted by supplying a mixed gas (50% H_2 and 50% H_2O) to a fuel electrode at the operating temperatures of 650, 700, and 750°C . The EC-mode I - V data of the SOC are presented in Fig. 6a. Both SOC exhibit OCV values of around 1.00, 0.98, and 0.96 V at the corresponding temperatures, in good agreement with the Nernst potentials (1.056, 1.049, and 1.042 V at 650, 700, and 750°C , respectively). The OCV values measured for the humidified condition (EC mode) also agree with the values obtained by various researchers under the same conditions (50% H_2 and 50% H_2O) [22–25, 29,33,69–71]. The I - V plots of the SOC with the nanolayered LSC air electrode exhibit a significant improvement in performance as compared to that of the SOC with the conventional LSC-GDC composite.

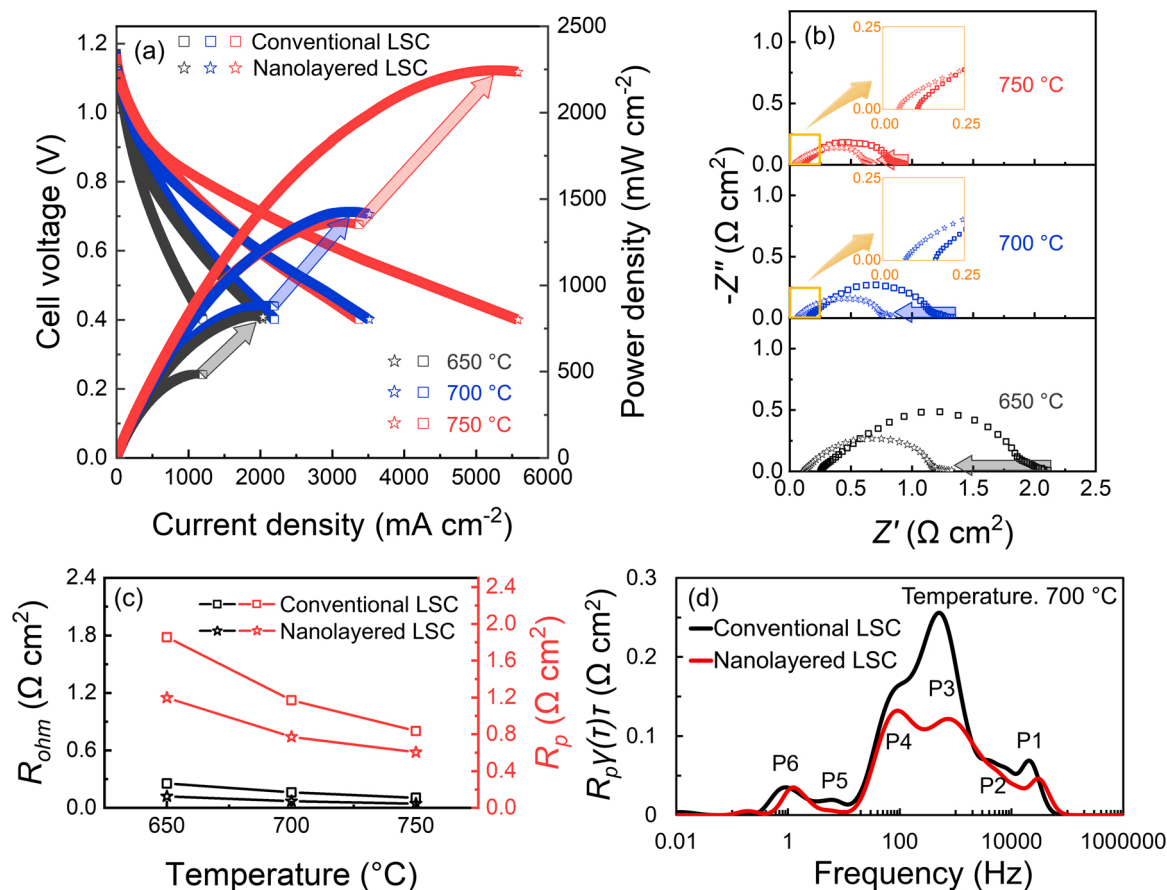


Fig. 5. FC performance comparison of SOCs with conventional LSC-GDC composite and nanolayered LSC air electrodes measured at different temperatures using dry hydrogen as a fuel and air as an oxidant: (a) I-V and I-P curves, (b) Nyquist plots of the AC-impedance spectra, (c) ohmic and polarization resistances, and (d) DRT plots obtained for the impedance data acquired at 700 °C.

At an operating voltage of 1.6 V, the SOC with the nanolayered LSC air electrode manifests maximum current density (MCD) values of 1.66, 2.75, and 4.57 A cm^{-2} at temperatures of 650, 700, and 750 °C, respectively, representing performance increments of 90.8%, 97.8%, and 107.7% in comparison to the conventional SOC. Fig. 6b and c provide a comparison of the AC-impedance data collected under OCV conditions for the two SOCs in the EC mode at different temperatures, indicating a remarkably improved activity of the nanolayered LSC air electrode. To explain the factors behind performance increment comprehensively, DRT plots derived from the impedance data are presented in Fig. 6d. Four distinct processes, P1 through P4, are apparent for the SOC with the conventional LSC-GDC composite air electrode, whereas P4 is not present for the SOC with the nanolayered LSC air electrode. Each of the processes can be explained subsequently, i.e., P1 is ionic conduction in MIEC, P2 is oxygen evolution at the air electrode, P3 is surface exchange on the air electrode and gas transport in the fuel electrode, whereas P4 explains the gas diffusion process inside the air electrode structure. For the SOC with the nanolayered LSC air electrode, the area under the entire DRT curve undergoes a significant reduction, indicating an enhancement in the kinetics of the air electrode processes. Particularly, the absence of P4 clearly shows that the air electrode decorated with the LSC nanolayer presents no resistance to the gas flow [72]. It is pertinent to notice that the MCD values of the SOC with the nanolayered LSC air electrode are amongst the highest reported values in the literature thus far, as summarized in Fig. 6e and Table S4. Furthermore, the SOC with nanolayered LSC air electrode outperforms all previously reported high performing SOCs in a high operating voltage region, i.e., 1.6 V [23–25,27,29,71,73]. In addition to this, as for FC-mode operation, the synthesis of the LSC air electrode as a nanolayer

lowers the operating temperature during EC-mode operation by ~ 50 °C.

3.6. Superior stability during reversible and long-term operations of SOC with nanolayered LSC air electrode

For practical applications, the SOC must possess high stability during long-term operations. An SOC reportedly undergoes severe degradation when operated in the EC mode, which can even result in delamination of the air electrode from the electrolyte. Therefore, durability measurements were conducted upon cycling between FC and EC modes. During this test, the SOCs were subjected to cycling between 500 mA cm^{-2} (EC mode) and -500 mA cm^{-2} (FC mode) at 700 °C, as shown in Fig. 7a and b. Cycling data of the SOC with the conventional LSC-GDC composite air electrode are illustrated in Fig. 7a. It is clear that the SOC performs poorly during the stability test, showing voltage fluctuations during cyclic operation and eventually breaking down after 23 cycles. Fig. 7d and S12 present post-test SEM images of the LSC-GDC composite air electrode after the durability tests. The air electrode was delaminated from the interface along the GDC buffer layer, which was rightly in accordance with other findings in the literature [12–14]. Cycling data of the SOC with the nanolayered LSC air electrode (Fig. 7b) demonstrate highly stable performance over 25 cycles without any voltage fluctuations. During operation in the FC mode, the SOC voltage increased from 0.83 V to 0.835 V, whereas in the EC mode, the initial and final voltages were recorded as 1.122 and 1.116 V, respectively. The SOC comprising of nanolayered LSC air electrode was further tested for its long-term durability in a galvanostatic operation, as shown in Fig. 7c. The SOC was first operated in the FC mode for 360 h at a current density of 500 mA cm^{-2} , demonstrating highly stable operation with voltage

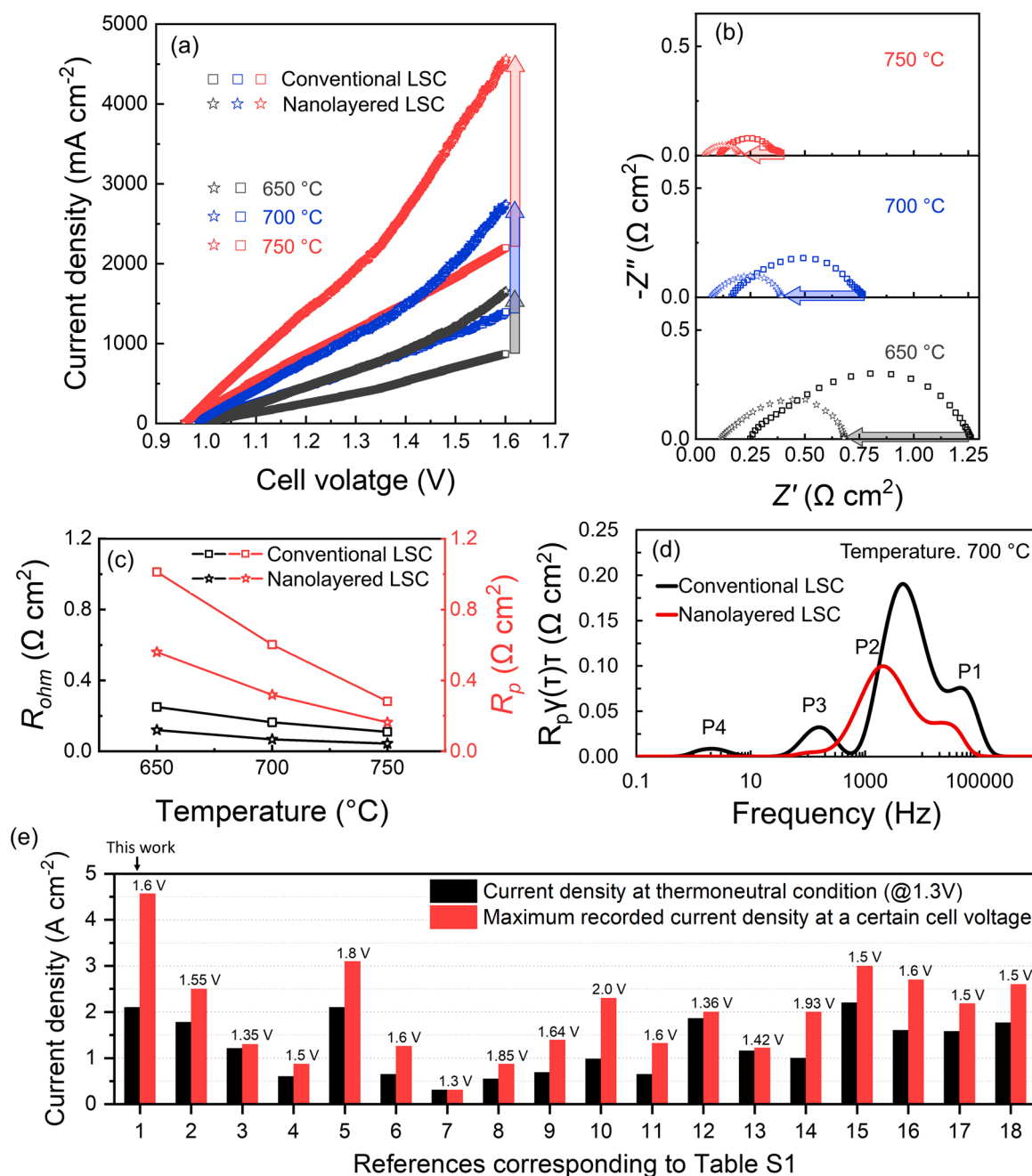


Fig. 6. EC performance comparison of SOCs with conventional LSC-GDC composite and nanolayered LSC air electrodes measured at different temperatures using a 50:50 hydrogen and steam mixture at the fuel electrode: (a) I-V curves, (b) Nyquist plots of the AC-impedance spectra, (c) ohmic and polarization resistances, (d) DRT plots of the impedance data obtained at 700 °C, and (e) performance comparison at 750 °C with data reported in literature (shown in Table S4).

variations ranging from 0.8330 to 0.8328 V. The SOC operation was then switched to the EC mode, and the applied current density was adjusted to obtain the thermoneutral condition, i.e., 1.3 V. In this case, a current density of $\sim 1100 \text{ mA cm}^{-2}$ was applied to obtain 1.3 V. The applied current density for the EC mode operation was kept constant for the next 340 h, where again the SOC showed highly stable operation with a performance enhancement as the cell voltage changed from 1.30 to 1.28 V. Fig. 7e shows a post-test SEM image of the SOC with the nanolayered LSC air electrode, validating that the air electrode maintained an intimately cohesive interface with the YSZ electrolyte without any signs of delamination. Post-test high-magnification SEM images were also taken from the nanolayered LSC air electrode, as shown in Fig. S13, which showed that the LSC nanoparticles were agglomerated slightly. However, no adverse effect was observed on the cell

performance during the long-term performance test. Furthermore, EC mode I-V curves (Fig. S14a) and Nyquist plots (Fig. S14b) obtained before and after the durability tests also verify the electrochemical performance increment of the SOC with the nanolayered LSC air electrode. Conclusively, the SOC consisting of a nanolayered LSC air electrode demonstrated exceedingly stable operation with no evidence of degradation during reversible cycling and galvanostatic durability tests, proving the superior robustness of the innovative SOC air electrode design.

4. Conclusion

In this study, we demonstrated the high FC-EC performance and reversible cycling durability of the SOC with the nanolayered LSC air

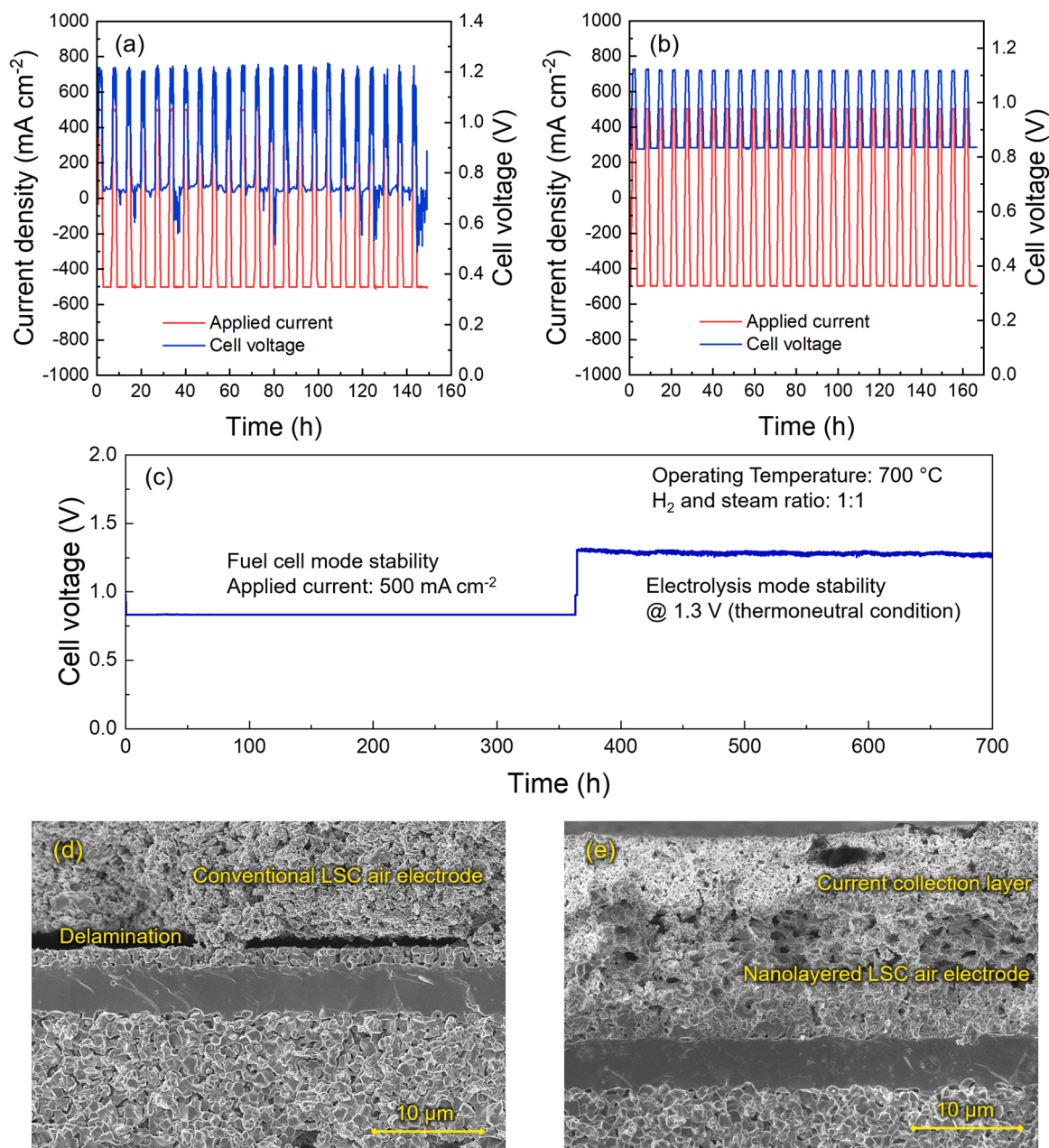


Fig. 7. Stability data of the SOCs obtained at an operating temperature of 700 °C and post-test SEM analysis. Cyclic FC-EC operations conducted between -500 and 500 mA cm^{-2} applied current densities of SOCs with (a) conventional LSC-GDC composite and (b) nanolayered LSC air electrodes. (c) Long-term galvanostatic operation in fuel cell and electrolysis modes of the SOC with nanolayered LSC air electrode. (d, e) Post-test cross-sectional SEM images of the SOCs with conventional and nanolayered LSC air electrodes, respectively.

electrode supported on the GDC scaffold with a graded porous structure. Superior performance is attributed to a greatly extended reaction area achieved by synthesizing LSC via the facile infiltration technique. The GDC buffer layer was also eliminated from the SOC structure, which leads to a reduced internal resistance of the SOC. Consequently, the operating temperature of the SOC was significantly reduced for the same level of performance when compared to a conventional LSC-GDC composite air electrode. More importantly, the critical issue of the air electrode delamination during EC-mode operations was successfully resolved. The excellent durability demonstrated here is attributed primarily to the formation of catalyst-free closed pores which alleviate the possibility for the entrapment of evolved O_2 gas, and also to the extremely fast diffusion properties of the LSC nanolayer. This study provides a comprehensive guideline for designing and controlling the

nano and microstructures of air electrodes to achieve high performance and durability for commercial applications of the next generation SOCs.

CRediT authorship contribution statement

Saeed Ur Rehman: Conceptualization, Design, Methodology, Investigation, Formal analysis, Writing – original draft. **Muhammad Haseeb Hassan:** Methodology, Writing, Editing. **Hye-Sung Kim:** Methodology, Investigation. **Rak-Hyun Song:** Investigation, Analysis, Resources. **Tak-Hyoung Lim:** Formal analysis, Investigation. **Jong-Eun Hong:** Formal analysis, Investigation. **Dong-Woo Joh:** Methodology, Investigation. **Seok-Joo Park:** Methodology, Editing. **Jong-Won Lee:** Investigation, Writing – review & editing. **Seung-Bok Lee:** Conceptualization, Resources, Supervision, Writing – review & editing.

Declaration of Competing Interest

The authors declare that they have no known competing financial interests or personal relationships that could have appeared to influence the work reported in this paper.

Data Availability

Data will be made available on request.

Acknowledgements

This work was supported by the Korea Institute of Energy Technology Evaluation and Planning (KETEP) and the Ministry of Trade, Industry & Energy (MOTIE) of the Republic of Korea (grant number 20213030030150). Moreover, this work was supported by the National Research Foundation (NRF) funded by the Ministry of Science and ICT (Grant number 2022M3H4A1A04076616).

Appendix A. Supporting information

Supplementary data associated with this article can be found in the online version at [doi:10.1016/j.apcatb.2023.122784](https://doi.org/10.1016/j.apcatb.2023.122784).

References

- G. Semieniuk, L. Taylor, A. Rezai, D.K. Foley, Plausible energy demand patterns in a growing global economy with climate policy, *Nat. Clim. Chang* 11 (2021) 313–318, <https://doi.org/10.1038/s41558-020-00975-7>.
- K.O. Yoro, M.O. Daramola, CO₂ Emission Sources, Greenhouse Gases, and the Global Warming Effect, in: *Adv. Carbon Capture*, Woodhead Publishing, 2020, pp. 3–28, <https://doi.org/10.1016/b978-0-12-819657-1.00001-3>.
- N. Keller, J. Ivanec, J. Highfield, A.M. Ruppert, Photo-/thermal synergies in heterogeneous catalysis: Towards low-temperature (solar-driven) processing for sustainable energy and chemicals, *Appl. Catal. B Environ.* 296 (2021), 120320, <https://doi.org/10.1016/j.apcatb.2021.120320>.
- A. Hauch, R. Küngas, P. Blennow, A.B. Hansen, J.B. Hansen, B.V. Mathiesen, M. B. Mogensen, Recent advances in solid oxide cell technology for electrolysis, *Science* 370 (80) (2020), <https://doi.org/10.1126/science.aba6118>.
- L. Ye, K. Xie, High-temperature electrocatalysis and key materials in solid oxide electrolysis cells, *J. Energy Chem.* 54 (2021) 736–745, <https://doi.org/10.1016/j.jechem.2020.06.050>.
- K. Hu, J. Fang, X. Ai, D. Huang, Z. Zhong, X. Yang, L. Wang, Comparative study of alkaline water electrolysis, proton exchange membrane water electrolysis and solid oxide electrolysis through multi-physics modeling, *Appl. Energy* 312 (2022), 118788, <https://doi.org/10.1016/j.apenergy.2022.118788>.
- Z. Chen, L. Jiang, S. He, C. Guan, Y. Zou, Z. Yue, N. Ai, S.P. Jiang, Y. Shao, K. Chen, Development of intertwined nanostructured multi-phase air electrodes for efficient and durable reversible solid oxide cells, *Appl. Catal. B Environ.* 305 (2022), 121056, <https://doi.org/10.1016/j.apcatb.2021.121056>.
- M.B. Mogensen, M. Chen, H.L. Frandsen, C. Graves, J.B. Hansen, K.V. Hansen, A. Hauch, T. Jacobsen, S.H. Jensen, T.L. Skafte, X. Sun, Reversible solid-oxide cells for clean and sustainable energy, *Clean. Energy* 3 (2019) 175–201, <https://doi.org/10.1093/ce/ckz023>.
- S.P. Jiang, Challenges in the development of reversible solid oxide cell technologies: a mini review, *Asia-Pac. J. Chem. Eng.* 11 (2016) 386–391, <https://doi.org/10.1002/apj.1987>.
- J. Zhang, S. Ricote, P.V. Hendriksen, Y. Chen, Advanced materials for thin-film solid oxide fuel cells: recent progress and challenges in boosting the device performance at low temperatures, *Adv. Funct. Mater.* (2022) 2111205, <https://doi.org/10.1002/adfm.202111205>.
- Y. Wang, W. Li, L. Ma, W. Li, X. Liu, Degradation of solid oxide electrolysis cells: phenomena, mechanisms, and emerging mitigation strategies—a review, *J. Mater. Sci. Technol.* 55 (2020) 35–55, <https://doi.org/10.1016/j.jmst.2019.07.026>.
- K. Chen, S.P. Jiang, Failure mechanism of (La,Sr)MnO₃ oxygen electrodes of solid oxide electrolysis cells, *Int. J. Hydrog. Energy* 36 (2011) 10541–10549, <https://doi.org/10.1016/j.ijhydene.2011.05.103>.
- M. Keane, M.K. Mahapatra, A. Verma, P. Singh, LSM-YSZ interactions and anode delamination in solid oxide electrolysis cells, *Int. J. Hydrog. Energy* 37 (2012) 16776–16785, <https://doi.org/10.1016/j.ijhydene.2012.08.104>.
- M.S. Sohal, J.E. O'Brien, C.M. Stoots, V.I. Sharma, B. Yildiz, A. Virkar, Degradation issues in solid oxide cells during high temperature electrolysis, in: *ASME 2010 8th Int. Conf. Fuel Cell Sci. Eng. Technol. FUELCCELL 2010*, American Society of Mechanical Engineers Digital Collection, 2010: pp. 377–387. (<https://doi.org/10.1115/FuelCell2010-33332>).
- C. Graves, S.D. Ebbesen, S.H. Jensen, S.B. Simonsen, M.B. Mogensen, Eliminating degradation in solid oxide electrochemical cells by reversible operation, *Nat. Mater.* 14 (2015) 239–244, <https://doi.org/10.1038/nmat4165>.
- A.V. Virkar, Mechanism of oxygen electrode delamination in solid oxide electrolyzer cells, *Int. J. Hydrog. Energy* 35 (2010) 9527–9543, <https://doi.org/10.1016/j.ijhydene.2010.06.058>.
- K. Chen, N. Ai, S.P. Jiang, Performance and stability of (La,Sr)MnO₃-Y₂O₃-ZrO₂ composite oxygen electrodes under solid oxide electrolysis cell operation conditions, *Int. J. Hydrog. Energy* 37 (2012) 10517–10525, <https://doi.org/10.1016/j.ijhydene.2012.04.073>.
- J. Kim, H. Il Ji, H.P. Dasari, D. Shin, H. Song, J.H. Lee, B.K. Kim, H.J. Je, H.W. Lee, K.J. Yoon, Degradation mechanism of electrolyte and air electrode in solid oxide electrolysis cells operating at high polarization, *Int. J. Hydrog. Energy* 38 (2013) 1225–1235, <https://doi.org/10.1016/j.ijhydene.2012.10.113>.
- J.R. Mawdsley, J. David Carter, A. Jeremy Kropf, B. Yildiz, V.A. Maroni, Post-test evaluation of oxygen electrodes from solid oxide electrolysis stacks, *Int. J. Hydrog. Energy* 34 (2009) 4198–4207, <https://doi.org/10.1016/j.ijhydene.2008.07.061>.
- M.A. Laguna-Bercero, R. Campana, A. Larrea, J.A. Kilner, V.M. Orera, Electrolyte degradation in anode supported microtubular yttria stabilized zirconia-based solid oxide steam electrolysis cells at high voltages of operation, *J. Power Sources* 196 (2011) 8942–8947, <https://doi.org/10.1016/j.jpowsour.2011.01.015>.
- S.N. Rashkeev, M.V. Glazoff, Atomic-scale mechanisms of oxygen electrode delamination in solid oxide electrolyzer cells, *Int. J. Hydrog. Energy* 37 (2012) 1280–1291, <https://doi.org/10.1016/j.ijhydene.2011.09.117>.
- H. Fan, M. Keane, N. Li, D. Tang, P. Singh, M. Han, Electrochemical stability of La_{0.6}Sr_{0.4}Co_{0.2}Fe_{0.8}O_{3-δ}-infiltrated YSZ oxygen electrode for reversible solid oxide fuel cells, *Int. J. Hydrog. Energy, Pergamon* (2014) 14071–14078, <https://doi.org/10.1016/j.ijhydene.2014.05.149>.
- T. Chen, Y. Zhou, M. Liu, C. Yuan, X. Ye, Z. Zhan, S. Wang, High performance solid oxide electrolysis cell with impregnated electrodes, *Electrochem. Commun.* 54 (2015) 23–27, <https://doi.org/10.1016/j.elecom.2015.02.015>.
- S. Il Lee, J. Kim, J.W. Son, J.H. Lee, B.K. Kim, H.J. Je, H.W. Lee, H. Song, K.J. Yoon, High performance air electrode for solid oxide regenerative fuel cells fabricated by infiltration of nano-catalysts, *J. Power Sources* 250 (2014) 15–20, <https://doi.org/10.1016/j.jpowsour.2013.10.123>.
- K. Joong Yoon, M. Biswas, H.J. Kim, M. Park, J. Hong, H. Kim, J.W. Son, J.H. Lee, B.K. Kim, H.W. Lee, Nano-tailoring of infiltrated catalysts for high-temperature solid oxide regenerative fuel cells, *Nano Energy* 36 (2017) 9–20, <https://doi.org/10.1016/j.nanoen.2017.04.024>.
- S. Kim, D.W. Joh, D.Y. Lee, J. Lee, H.S. Kim, M.Z. Khan, J.E. Hong, S.B. Lee, S. J. Park, R.H. Song, M.T. Mehran, C.K. Rhee, T.H. Lim, Microstructure tailoring of solid oxide electrolysis cell air electrode to boost performance and long-term durability, *Chem. Eng. J.* 410 (2021), 128318, <https://doi.org/10.1016/j.cej.2020.128318>.
- X. Tong, Y. Xu, D. Tripković, P.V. Hendriksen, W.R. Kiebach, M. Chen, Promotion of oxygen reduction and evolution by applying a nanoengineered hybrid catalyst on cobalt free electrodes for solid oxide cells, *J. Mater. Chem. A* 8 (2020) 9039–9048, <https://doi.org/10.1039/d0ta02979c>.
- K. Chen, N. Ai, S.P. Jiang, Reasons for the high stability of nano-structured (La,Sr) MnO₃ infiltrated Y₂O₃-ZrO₂ composite oxygen electrodes of solid oxide electrolysis cells, *Electrochem. Commun.* 19 (2012) 119–122, <https://doi.org/10.1016/j.elecom.2012.03.033>.
- S.L. Zhang, H. Wang, M.Y. Lu, C.X. Li, C.J. Li, S.A. Barnett, Electrochemical performance and stability of SrTi_{0.3}Fe_{0.6}Co_{0.1}O_{3-δ} infiltrated La_{0.8}Sr_{0.2}MnO₃-ZrO₂Y₂O₃ oxygen electrodes for intermediate-temperature solid oxide electrochemical cells, *J. Power Sources* 426 (2019) 233–241, <https://doi.org/10.1016/j.jpowsour.2019.04.044>.
- H. Fan, M. Han, Electrochemical stability of Sm_{0.5}Sr_{0.5}CoO_{3-δ}-infiltrated YSZ for solid oxide fuel cells/electrolysis cells, *Faraday Discuss.* 182 (2015) 477–491, <https://doi.org/10.1039/c5fd00022j>.
- Y. Wang, Z. Yang, M. Han, J. Chang, Optimization of Sm_{0.5}Sr_{0.5}CoO_{3-δ}-infiltrated YSZ electrodes for solid oxide fuel cell/electrolysis cell, *RSC Adv.* 6 (2016) 112253–112259, <https://doi.org/10.1039/c6ra21200j>.
- H. Fan, Y. Zhang, M. Han, Infiltration of La_{0.6}Sr_{0.4}FeO_{3-δ} nanoparticles into YSZ scaffold for solid oxide fuel cell and solid oxide electrolysis cell, *J. Alloy. Compd.* 723 (2017) 620–626, <https://doi.org/10.1016/j.jallcom.2017.06.018>.
- X. Tong, S. Ovtar, K. Brodersen, P.V. Hendriksen, M. Chen, A 4 × 4 cm² nanoengineered solid oxide electrolysis cell for efficient and durable hydrogen production, *ACS Appl. Mater. Interfaces* 11 (2019) 25996–26004, <https://doi.org/10.1021/acsami.9b07749>.
- S.U. Rehman, H.S. Song, H.S. Kim, M.H. Hassan, D.W. Joh, R.H. Song, T.H. Lim, J. E. Hong, S.J. Park, S.B. Lee, A dynamic infiltration technique to synthesize nanolayered cathodes for high performance and robust solid oxide fuel cells, *J. Energy Chem.* 70 (2022) 201–210, <https://doi.org/10.1016/j.jechem.2022.02.052>.
- Y.H. Song, S.U. Rehman, H.S. Kim, H.S. Song, R.H. Song, T.H. Lim, J.E. Hong, S. J. Park, J.Y. Huh, S.B. Lee, Facile surface modification of LSCF/GDC cathodes by epitaxial deposition of Sm_{0.5}Sr_{0.5}CoO₃ via ultrasonic spray infiltration, *J. Mater. Chem. A* 8 (2020) 3967–3977, <https://doi.org/10.1039/c9ta11704k>.
- H.A. Ishfaq, M.Z. Khan, M.T. Mehran, R. Raza, W.H. Tanveer, S. Bibi, A. Hussain, H.A. Muhammad, R.H. Song, Boosting performance of the solid oxide fuel cell by facile nano-tailoring of La_{0.6}Sr_{0.4}CoO_{3-δ} cathode, *Int. J. Hydrog. Energy* 47 (2022) 37587–37598, <https://doi.org/10.1016/j.ijhydene.2021.11.109>.
- E.N. Armstrong, K.L. Duncan, E.D. Wachsmann, Effect of A and B-site cations on surface exchange coefficient for ABO₃ perovskite materials, *Phys. Chem. Chem. Phys.* 15 (2013) 2298–2308, <https://doi.org/10.1039/c2cp42919e>.
- T. Lehtinen, M. Noponen, Solid oxide electrolyser demonstrator development at elcogen, *ECS Meet. Abstr. MA2021-03* (2021), <https://doi.org/10.1149/ma2021-031285mtgabs>, 285–285.

- [39] M. Noponen, P. Torri, J. Göös, J. Puranen, T. Lehtinen, S. Pylpko, E. Ounpuu, Progress of SOC Development at Elcogen, 189–189, ECS Meet. Abstr. MA2021-03 (2021), <https://doi.org/10.1149/ma2021-031189mtgabs>.
- [40] N.P. Bansal, Z. Zhong, Combustion synthesis of $\text{Sm}_{0.5}\text{Sr}_{0.5}\text{CoO}_{3-x}$ and $\text{La}_{0.6}\text{Sr}_{0.4}\text{CoO}_{3-x}$ nanopowders for solid oxide fuel cell cathodes, *J. Power Sources* 158 (2006) 148–153, <https://doi.org/10.1016/j.jpowsour.2005.09.057>.
- [41] T.Z. Shoklapper, C. Lu, C.P. Jacobson, S.J. Visco, L.C. De Jonghe, LSM-infiltrated solid oxide fuel cell cathodes, *Electrochem. Solid-State Lett.* 9 (2006) A376, <https://doi.org/10.1149/1.2206011>.
- [42] S.U. Rehman, H.S. Song, H.S. Kim, M.H. Hassan, D.W. Joh, R.H. Song, T.H. Lim, J. E. Hong, S.J. Park, S.B. Lee, A dynamic infiltration technique to synthesize nanolayered cathodes for high performance and robust solid oxide fuel cells, *J. Energy Chem.* 70 (2022) 201–210, <https://doi.org/10.1016/j.jechem.2022.02.052>.
- [43] K. Develos-Bagarinao, R.A. Budiman, S.S. Liu, T. Ishiyama, H. Kishimoto, K. Yamaji, Evolution of cathode-interlayer interfaces and its effect on long-term degradation, *J. Power Sources* 453 (2020), 227894, <https://doi.org/10.1016/j.jpowsour.2020.227894>.
- [44] Y. Gu, Y. Zhang, Y. Zheng, H. Chen, L. Ge, L. Guo, $\text{PrBaMn}_{2}\text{O}_{5+\Delta}$ with praseodymium oxide nano-catalyst as electrode for symmetrical solid oxide fuel cells, *Appl. Catal. B Environ.* 257 (2019), 117868, <https://doi.org/10.1016/j.apcatb.2019.117868>.
- [45] S.U. Rehman, A. Shaur, H.S. Kim, D.W. Joh, R.H. Song, T.H. Lim, J.E. Hong, S. J. Park, S.B. Lee, Effect of transition metal doping on the sintering and electrochemical properties of GDC buffer layer in SOFCs, *Int. J. Appl. Ceram. Technol.* 18 (2021) 511–524, <https://doi.org/10.1111/ijac.13650>.
- [46] Y.C. Wu, P.Y. Huang, G. Xu, Properties and microstructural analysis of $\text{La}_{1-x}\text{Sr}_x\text{CoO}_{3-\delta}$ ($x=0-0.6$) cathode materials, *Ceram. Int.* 43 (2017) 2460–2470, <https://doi.org/10.1016/j.ceramint.2016.11.041>.
- [47] S.U. Rehman, R.H. Song, T.H. Lim, S.J. Park, J.E. Hong, J.W. Lee, S.B. Lee, High-performance nanofibrous LaCoO_3 perovskite cathode for solid oxide fuel cells fabricated: Via chemically assisted electrodeposition, *J. Mater. Chem. A* 6 (2018) 6987–6996, <https://doi.org/10.1039/c7ta10701c>.
- [48] S.U. Rehman, A. Shaur, R.H. Song, T.H. Lim, J.E. Hong, S.J. Park, S.B. Lee, Nano-fabrication of a high-performance LaNiO_3 cathode for solid oxide fuel cells using an electrochemical route, *J. Power Sources* 429 (2019) 97–104, <https://doi.org/10.1016/j.jpowsour.2019.05.007>.
- [49] Z. Gao, E.C. Miller, S.A. Barnett, A high power density intermediate-temperature solid oxide fuel cell with thin ($\text{La}_{0.9}\text{Sr}_{0.1}\text{O}_{3-\delta}$ ($\text{Ga}_{0.8}\text{Mg}_{0.2}\text{O}_{3-\delta}$) electrolyte and nano-scale anode, *Adv. Funct. Mater.* 24 (2014) 5703–5709, <https://doi.org/10.1002/adfm.201400295>.
- [50] A. Athanasiou, A. Mitsionis, T. Vaimakis, P. Pomonis, D. Petrakis, L. Loukatzikou, N. Todorova, C. Trapalis, S. Ladasc, A novel route for the production of TiO_2 photocatalysts with lowenergy gap, via Triton-X and oleic acid surfactants, *Appl. Surf. Sci.* 319 (2014) 143–150, <https://doi.org/10.1016/j.apsusc.2014.06.086>.
- [51] E. Iyyappan, P. Wilson, Synthesis of nanoscale hydroxyapatite particles using triton X-100 as an organic modifier, *Ceram. Int.* 39 (2013) 771–777, <https://doi.org/10.1016/j.ceramint.2012.06.090>.
- [52] T.E. Burye, J.D. Nicholas, Nano-ceria pre-infiltration improves $\text{La}_{0.6}\text{Sr}_{0.4}\text{Co}_{0.8}\text{Fe}_{0.2}\text{O}_{3-x}$ infiltrated solid oxide fuel cell cathode performance, *J. Power Sources* 300 (2015) 402–412, <https://doi.org/10.1016/j.jpowsour.2015.09.080>.
- [53] J.D. Nicholas, S.A. Barnett, Measurements and modeling of $\text{Sm}_{0.5}\text{Sr}_{0.5}\text{CoO}_{3-x}$ - $\text{Ce}_{0.9}\text{Gd}_{0.1}\text{O}_{1.95}$ SOFC cathodes produced using infiltrate solution additives, *J. Electrochem. Soc.* 157 (2010) B536, <https://doi.org/10.1149/1.3284519>.
- [54] T.E. Burye, J.D. Nicholas, Precursor solution additives improve desiccated $\text{La}_{0.6}\text{Sr}_{0.4}\text{Co}_{0.8}\text{Fe}_{0.2}\text{O}_{3-x}$ infiltrated solid oxide fuel cell cathode performance, *J. Power Sources* 301 (2016) 287–298, <https://doi.org/10.1016/j.jpowsour.2015.10.012>.
- [55] R.P. Dowd, S. Lee, Y. Fan, K. Gerdes, Engineering the solid oxide fuel cell electrocatalyst infiltration technique for industrial use, *Int. J. Hydrog. Energy* 41 (2016) 14971–14981, <https://doi.org/10.1016/j.ijhydene.2016.06.015>.
- [56] J. Januschewsky, M. Ahrens, A. Opitz, F. Kubel, J. Fleig, Optimized $\text{La}_{0.6}\text{Sr}_{0.4}\text{CoO}_{3-\delta}$ thin-film electrodes with extremely fast oxygen-reduction kinetics, *Adv. Funct. Mater.* 19 (2009) 3151–3156, <https://doi.org/10.1002/adfm.200900362>.
- [57] T. Kawada, K. Masuda, J. Suzuki, A. Kaimai, K. Kawamura, Y. Nigara, J. Mizusaki, H. Yugami, H. Arashi, N. Sakai, H. Yokokawa, Oxygen isotope exchange with a dense $\text{La}_{0.6}\text{Sr}_{0.4}\text{CoO}_{3-\delta}$ electrode on a $\text{Ce}_{0.9}\text{Ca}_{0.1}\text{O}_{1.9}$ electrolyte, *Solid State Ion.* 121 (1999) 271–279, [https://doi.org/10.1016/S0167-2738\(99\)00046-6](https://doi.org/10.1016/S0167-2738(99)00046-6).
- [58] Y. Takeda, R. Kanno, M. Noda, O. Yamamoto, Perovskite electrodes for high temperature solid electrolyte fuel cells (commemoration issue dedicated to professor Toshio TAKADA on the occasion of his retirement) perovskite electrodes for high temperature solid electrolyte fuel cells, *Bull. Inst. Chem. Res., Kyoto Univ.* 64 (1986). (<http://hdl.handle.net/2433/77164>) (accessed April 28, 2022).
- [59] E. Mutoro, E.J. Crumlin, M.D. Biegalski, H.M. Christen, Y. Shao-Horn, Enhanced oxygen reduction activity on surface-decorated perovskite thin films for solid oxide fuel cells, *Energy Environ. Sci.* 4 (2011) 3689–3696, <https://doi.org/10.1039/c1ee01245b>.
- [60] M. Choolaei, Q. Cai, R.C.T. Slade, B. Amini Horri, Nanocrystalline gadolinium-doped ceria (GDC) for SOFCs by an environmentally-friendly single step method, *Ceram. Int.* 44 (2018) 13286–13292, <https://doi.org/10.1016/j.ceramint.2018.04.159>.
- [61] N. Van Minh, Raman Scattering Study of Perovskite Manganites, in: *J. Phys. Conf. Ser.*, IOP Publishing, 2009, 012011, <https://doi.org/10.1088/1742-6596/187/1/012011>.
- [62] X. Li, K. Blinn, Y. Fang, M. Liu, M.A. Mahmoud, S. Cheng, L.A. Bottomley, M. El-Sayed, M. Liu, Application of surface enhanced Raman spectroscopy to the study of SOFC electrode surfaces, *Phys. Chem. Chem. Phys.* 14 (2012) 5919–5923, <https://doi.org/10.1039/c2cp40091j>.
- [63] L. Zhao, J. Zhang, T. Becker, S.P. Jiang, Raman spectroscopy study of chromium deposition on $\text{La}_{0.6}\text{Sr}_{0.4}\text{Co}_{0.2}\text{Fe}_{0.8}\text{O}_{3-\delta}$ cathode of solid oxide fuel Cells, *J. Electrochem. Soc.* 161 (2014) F687–F693, <https://doi.org/10.1149/2.018406jes>.
- [64] A. Ishikawa, J. Nohara, S. Sugai, Raman study of the orbital-phonon coupling in LaCoO_3 , *Phys. Rev. Lett.* 93 (2004), 136401, <https://doi.org/10.1103/PhysRevLett.93.136401>.
- [65] H. Sumi, H. Shimada, Y. Yamaguchi, T. Yamaguchi, Y. Fujishiro, Degradation evaluation by distribution of relaxation times analysis for microtubular solid oxide fuel cells, *Electrochim. Acta* 339 (2020), 135913, <https://doi.org/10.1016/j.electacta.2020.135913>.
- [66] P. Caliendo, A. Nakajo, S. Diethelm, J. Van herle, Model-assisted identification of solid oxide cell elementary processes by electrochemical impedance spectroscopy measurements, *J. Power Sources* 436 (2019), 226838, <https://doi.org/10.1016/j.jpowsour.2019.226838>.
- [67] J. Hong, A. Bhardwaj, H. Bae, I. Kim, S.-J. Song, Electrochemical impedance analysis of SOFC with transmission line model using distribution of relaxation times (DRT), *J. Electrochem. Soc.* 167 (2020), 114504, <https://doi.org/10.1149/1945-7111/aba00f>.
- [68] Y. Niu, Y. Zhou, W. Lv, Y. Chen, Y. Zhang, W. Zhang, Z. Luo, N. Kane, Y. Ding, L. Soule, Y. Liu, W. He, M. Liu, Enhancing oxygen reduction activity and Cr tolerance of solid oxide fuel cell cathodes by a multiphase catalyst coating, *Adv. Funct. Mater.* 31 (2021) 2100034, <https://doi.org/10.1002/adfm.202100034>.
- [69] M.J. López-Robledo, M.A. Laguna-Bercero, A. Larrea, V.M. Orea, Reversible operation of microtubular solid oxide cells using $\text{La}_{0.6}\text{Sr}_{0.4}\text{Co}_{0.2}\text{Fe}_{0.8}\text{O}_{3-\delta}$ - $\text{Ce}_{0.9}\text{Gd}_{0.1}\text{O}_{2-\delta}$ oxygen electrodes, *J. Power Sources* 378 (2018) 184–189, <https://doi.org/10.1016/j.jpowsour.2017.12.035>.
- [70] T. Chen, M. Liu, C. Yuan, Y. Zhou, X. Ye, Z. Zhan, C. Xia, S. Wang, High performance of intermediate temperature solid oxide electrolysis cells using $\text{Nd}_2\text{NiO}_{4+\delta}$ impregnated scandia stabilized zirconia oxygen electrode, *J. Power Sources* 276 (2015) 1–6, <https://doi.org/10.1016/j.jpowsour.2014.11.042>.
- [71] S.L. Zhang, H. Wang, M.Y. Lu, A.P. Zhang, L.V. Mogni, Q. Liu, C.X. Li, C.J. Li, S. A. Barnett, Cobalt-substituted $\text{SrTi}_{0.3}\text{Fe}_{0.7}\text{O}_{3-\delta}$ a stable high-performance oxygen electrode material for intermediate-temperature solid oxide electrochemical cells, *Energy Environ. Sci.* 11 (2018) 1870–1879, <https://doi.org/10.1039/c8ee00449h>.
- [72] X. Tong, S. Ovtar, K. Brodersen, P.V. Hendriksen, M. Chen, A $4 \times 4 \text{ cm}^2$ nanoengineered solid oxide electrolysis cell for efficient and durable hydrogen production, *ACS Appl. Mater. Interfaces* 11 (2019) 25996–26004, <https://doi.org/10.1021/acsami.9b07749>.
- [73] S.L. Zhang, D. Cox, H. Yang, B.K. Park, C.X. Li, C.J. Li, S.A. Barnett, High stability $\text{SrTi}_{1-x}\text{Fe}_x\text{O}_{3-\delta}$ electrodes for oxygen reduction and oxygen evolution reactions, *J. Mater. Chem. A* 7 (2019) 21447–21458, <https://doi.org/10.1039/c9ta07548h>.